A&A manuscript no.
(will be inserted by hand later)

Your thesaurus codes are:
08.14.2.; 08.02.2; 08.13.1; 08.09.2 V2301 Oph)

ASTRONOMY
AND
ASTROPHYSICS
22.8.1997

Spectroscopic and spectrophotometric studies of V2301 Oph – I.The high accretion state ⋆

Damir Šimić, Heinz Barwig, Andreas Bobinger, Karl–Heinz Mantel, and Sebastian Wolf

Universitäts-Sternwarte, Scheinerstr. 1, 81679 München, Germany

Received: April 14, 1997; Accepted: August 8, 1997

Abstract. An approach is made to clarify the two different classifications of V2301 Oph (formerly: 1H1752+081) as a low field intermediate polar or an AM Her candidate, by analysing phase–resolved spectroscopy and simultaneously recorded high–speed–spectrophotometry. By combining both data sets we obtained for the first time photometric data of V2301 Oph with high spectral (1.3Å) resolution during an enhanced accretion state. The trailed spectrograms show in unprecedented clearness the well–known complex emission line profiles which are characterized by a broad and a narrow component shifted in phase by $\Delta\varphi \approx 0.25$. By means of Doppler tomography the origin of the narrow component can be located on the irradiated face of the secondary star, whereas the broad component can be traced back to the coupling region where the accreting material is connected to the field lines.

It was also possible to analyse separately the eclipse behaviour of the emission lines and of the respective continua. The decomposed continuum light–curves clearly reveal that the pre–eclipse hump cannot be explained with a hot spot on an accretion disk. It can be rather assigned to cyclotron radiation from a shock–region on the white dwarf. Furthermore, it is shown from the eclipse features, that the acccretion stream is distorted due to a weak magnetic field. An investigation of the superimposed flickering did not reveal any short–periodic variation, which would be an evidence for a non–synchronuosly rotating primary star. Therefore, we can classify V2301 Oph as an AM Her system, where the dipole axis of the white dwarf is inclined to its rotational axis.

Key words: stars: individual: V2301 Oph – cataclysmic variables – eclipsing binaries – stars: magnetic fields

Send offprint requests to: Damir Šimić (*e–mail: simic@usm.uni-muenchen.de*)

⋆ Based on observations obtained at the German–Spanish Astronomical Center, Calar Alto, Spain.

1. Introduction

The X–ray source V2301 Oph (formerly: 1H1752+081) discovered during the HEAO–1 Modulation Collimator survey turned out to be an eclipsing cataclysmic variable (CV) with an orbital period of 1.88 h (Silber et al. 1994).

Different approaches were made to analyse and classify this unique binary system. Silber (1992) performed optical spectroscopy and CCD–photometry of V2301 Oph in a high accretion state, concluding that this CV may be a DQ Her type binary with a small accretion disc. Barwig et al. (1994) independently obtained spectroscopic and photometric data in 1992 and suggested that this system is an AM Her type eclipsing binary without an accretion disc. Ferrario et al. (1995) undertook spectropolarimetric observations of V2301 Oph in a low accretion state and found out that the white dwarf has a magnetic field structure that deviates from that of a centered dipole with a measured mean photospheric field of about 7 MG. Therefore, they argued this binary system being probably a low–field AM Her variable. According to Antipin & Shugarov (1995) this CV exhibits regular light variations with a 148.3 d period. The authors concluded that these long–term light variations (up to 1^m) might be due to large–scale changes in the accretion rate on the white dwarf which switches between high and low accretion states.

AM Herculis systems are close binary systems containing a late type secondary star and a strong magnetic white dwarf primary star. Material escapes from the Roche lobe filling secondary star and accretes along the magnetic field lines onto the primary star, without forming an accretion disc. This happens, because the white dwarf, due to its strong magnetic field, is locked into synchronous rotation with the orbital period. Depending on the dipole inclination, accretion can occur onto one or two regions which are located on opposite hemispheres of the white dwarf (Ferrario et al. 1989). Intermediate polars (high and low field IPs) show a different behaviour, because their magnetic field is considerably weaker than those of AM Hers. As a result, the white dwarf is not synchronously rotating with the orbital period. Still, material can accrete onto the white dwarf (high field IPs) without creating an accretion disc.

The magnetically funnelled material streams onto the pole which is inclinated towards the incoming stream, so that each magnetic pole accretes material for half a beat–cycle, causing a pole–switching type modulation (Ferrario et al. 1993). Low field intermediate polars can form a partial accretion disc, where most of the energy of the incoming accretion stream is spread by viscous forces in the disc. Assuming again an oblique magnetic dipole of the white dwarf, accretion processes can only happen onto one of the two foot points of a field line which connects the coupling region to the primary star. Therefore, two accretion curtains are formed, one below and one above the orbital plane extended by 180^0 in longitude, where material is accreted along the field lines (Ferrario & Wickramasinghe 1993).

This paper intends to examine the two different classifications (AM Her versus IPs) by analysing simultaneously taken spectroscopic and spectrophotometric data sets when the system was in a high accretion state. The different on/off conditions of the accretion process enable us either to study the properties of the gas–stream and the reprocessing effects involved (this paper) or to study the primary and secondary star, because the stream emission lines are considerably weaker, so that absorption lines from the secondary can be detected and examined (Paper II, Barwig, in preparation).

In Sect. 2 we refer on the spectroscopic and spectrophotometric observations of V2301 Oph and the data reduction procedures used. Section 3 deals with the results and analysis of the data sets. In Sect. 4 we present a discussion and our conclusions.

2. Data acquisition and reduction

A special approach to investigate V2301 Oph was made during the observing campaign in August 1994. We performed simultaneous spectroscopy and spectrophotometry, respectively at the 3.5m and 2.2m telescopes at the German–Spanish Astronomical Center, Calar Alto, Spain.

2.1. Spectroscopy

V2301 Oph was observed on August 06–09, 1994 with the Cassegrain double beam spectrograph (TWIN) attached to the 3.5m telescope. The blue and the red spectral channels were equipped with low–noise CCDs (TEK#11 and TEK#12) with a pixel size of $24\mu m$ and a CCD size of 1024x1024 pixel. Using a slit–width of $1.''5$ and a spectral resolution of 1.3Å, we chose the spectral range of $4080\ldots5430$Å in the blue and $6500\ldots8400$Å in the red. The object was trailed along the slit, in order to obtain phase–resolved, high resolution spectra. Exposure times ranged between $300\ldots1800$s and the mean trail velocity amounted to 1pixel/22s. The trailed spectra were binned in direction of the slit by a factor of 2. Flatfield measurements were taken at the beginning and end of each night, as well as Helium–Argon wavelength calibration spectra which were taken approximately every hour during the night. Further information about the observation is given in Table 1. The data reduction included bias–subtraction, flatfield–correction, sky–subtraction, cosmic–ray elimination and wavelength–calibration as described in e.g. Horne (1986). After that, the continuum of the spectroscopic data set was calibrated, with our simultaneously obtained spectrophotometric data. By applying this method we were able to correct for intensity variations of the emission lines which might have been caused by poor weather conditions (e.g clouds) or observational difficulties (e.g. variable vignetting of the seeing disc by the slit). This new method which allows a relatively precise determination of the emission line flux is described in the next section.

In a last step the trailed spectra were phase–folded into 100 phase bins using an update of the eclipse–ephemeris of V2301 Oph given by Barwig et al. (1994) :

HJD 2448071.02014 (±7) + 0.078450008 $(\pm10)\times$ E

2.2. Spectrophotometry

Simultaneously with the spectroscopic measurements, we obtained high–speed (time resolution : 1s) spectrophotometric data with MEKASPEK attached to the 2.2m telescope at the Calar Alto Observatory. This 4 channel fiber–optic spectrophotometer was developed at the Universitäts–Sternwarte München and has the following properties :

Simultaneous measurements of object, two comparison stars and sky background within the spectral range of $3700\ldots9000$Å at a spectral resolution of $\lambda\ /\ \Delta\lambda \approx 50$. The photon–counting two–dimensional detector (MEPSICRON) has an time resolution of up to 20ms with no deadtime during readout.

Furthermore, MEKASPEK performs a correct treatment of atmospheric extinction effects and allows an accurate colour transformation to any broadband photometric system. A specially developed online–graphics–system allows to examine in realtime the observed spectra and light curves of object, comparison stars and sky background in selected spectral regions. For more details see Mantel et al. (1993b) and Mantel & Barwig (1993). Atmospheric effects are eliminated using the so–called $standard\ reduction$ (Barwig et al. 1987) which subtracts the sky background of each colour channel from object and comparison star and divides the object by the comparison star measurements afterwards, therefore enabling photometric measurements even under non–photometric conditions.

A new method for calibrating the trailed spectra with the spectrophotometric data set resulted from the above mentioned advantages of multichannel photometry.

Before this procedure could be employed, the continuum of the spectra had to be normalized by dividing it with undisturbed continuum ranges, where no line features (emission lines or absorption bands) appeared. By interpolating between those areas afterwards, we could normalize the data set in the entire spectral range.

From our spectrophotometric data set, narrow–band, filter–curves were extracted from the continuum in the same spectral ranges that were used to normalize the spectroscopic data.

The following multiplication with the reduced narrow–band data allows a calibration of the spectra.

Our continuum filter–curves can be used, after multiplication, in the same way for interpolation between the designated areas in order to calibrate the entire spectral range.
Due to the properties of MEKASPEK, it is also possible to investigate separately the Balmer emission lines and the respective continua. However, because of the short integration time (1s) the single spectra are quite weak. In order to improve the S/N, the spectra were binned in time by a factor of 20. Instead of dividing by the comparison star, we confined the reduction to sky–subtraction only. Non–photometric parts of light curves were excluded. The emission lines were extracted from the spectrophotometric data set by subtracting an interpolated continuum. Therewith, we are enabled to investigate information that might be included either in the continuum or in the emission lines.
As mentioned before, the spectrophotometric and spectroscopic data sets were taken simultaneously, except the nights of 04–05 August 1994, when the MEKASPEK team received additional observing time. Due to instrumental difficulties, no data could be obtained during the night of 05/06.08.1994. The observational details are listed in Table 2.

Table 1. Journal of spectroscopic observations. B = blue spectral region, R = red spectral region, UT=universal time, IT=integration time

Date	Spectra	Phase range	Start (UT)	IT (s)
06/07.08.1994	B R	0.21–0.48	$21^h20^m40^s$	1800
	B R	0.53–0.72	$21^h56^m49^s$	1300
	B R	0.78–0.88	$22^h25^m03^s$	600
	B R	0.92–0.18	$22^h40^m25^s$	1800
	B R	0.23–0.49	$23^h15^m52^s$	1800
07/08.08.1994	B R	0.93–0.04	$21^h17^m10^s$	760
	B R	0.50–0.61	$22^h21^m34^s$	785
	B R	0.47–0.64	$00^h11^m50^s$	1200
	B R	0.70–0.79	$00^h36^m51^s$	635
	B R	0.86–0.90	$00^h55^m12^s$	300
	B R	0.94–0.04	$01^h04^m18^s$	720
08/09.08.1994	B R	0.49–0.67	$20^h56^m30^s$	1200
	B	0.74–0.85	$21^h24^m54^s$	721
	B R	0.20–0.37	$22^h16^m29^s$	1200
	B R	0.41–0.60	$22^h40^m52^s$	1200
	B R	0.64–0.83	$23^h05^m53^s$	1300
	B R	0.89–0.10	$23^h33^m55^s$	1500

Table 2. Journal of spectrophotometric observations. UT=universal time, IT=integration time

Date	Start (UT)	Stop (UT)	IT (s)
04/05.08.1994	$20^h54^m04^s$	$23^h10^m44^s$	1
06/07.08.1994	$20^h40^m41^s$	$23^h39^m49^s$	1
07/08.08.1994	$20^h23^m58^s$	$01^h23^m24^s$	1
08/09.08.1994	$20^h28^m43^s$	$00^h02^m54^s$	1

3. Analysis and results

3.1. The trailed spectra

A detailed survey of individual emission lines, that is to say, the stronger lines H_δ, H_γ, H_β, H_α, HeI ($\lambda\lambda\,4471,\ 6686\ ,7065$), HeII ($\lambda\,4686$) are shown in Fig. 1, all with a phase resolution of 100 phase bins. The dynamical gray–scale range was set intentionally, in order to emphasize the individual line features. The emission lines of HeI (($\lambda\lambda\,4921, 5015$) blended with FeI ($\lambda\lambda\,4924, 5018$)), were excluded from further investigations due to the poor S/N.
With the exception of HeII (λ 4686) and HeI (λ 7065) all emission lines exhibit the same general appeareance, a broad component (henceforth BC) and a narrow component (henceforth NC). It is generally assumed that the multiple emission lines in AM Hers are produced in different parts of the accretion stream (BC) and on the X–ray–heated surface of the secondary star (NC). Comprehensive discussions about the emission line origins can be found in Young & Schneider (1979) or Biermann et al. (1985). A number of various authors (e.g. Rosen et al. 1987; Schwope et al. 1996) have presented analysis of AM Her stars with complex phase–dependent emission line profiles which confirm the theoretical assumptions.
The origin of the BC of V2301 Oph can be assigned to the accretion stream which is free–falling from the inner Lagrangian point L_1 towards the white dwarf, until it is compressed in the coupling region, where the accreting material is connected to the magnetic field lines of the primary star. From there on, the gas–stream is funneled along the magnetic field lines, until it impacts onto the surface of the white dwarf, creating an accretion spot or a so–called post–shock region (Mukai, 1988). The orbital intensity variations of the BC can be explained geometrically, assuming an optically thick accretion stream. Betweeen phases $\varphi = 0.05 \ldots 0.35$ the inner, illuminated concave side of the gas stream facing the primary star is moving towards maximum approaching velocity ($\varphi \approx 0.46$). During the phase–ranges between $\varphi = 0.4 \ldots 0.5$ a significant decrease of intensity is observed when the BC is probably eclipsed by itself. The eclipse of the emission lines ocurring around phase $\varphi \approx 0.0$ is total.
In favour of this interpretation, is the fact that the lines show no sign of a rotational disturbance and the mean orbital spectra presented in Fig.2 show only single peaked emission lines. Both signatures make it rather unlikely that an accretion disc is present in V2301 Oph as proposed by Silber et al. (1992).
Another criterion in favour of an AM Her classification is the absence of any outbursts. Antipin & Shugarov (1995) reported the existence of regular light variations with a 148.3 d period, which are due to changes in the accretion rate on the primary star. The resulting high/low states are characteristic of the long–term variability of AM Hers.
The origin of the NC can be found on the hemisphere of the secondary star facing the white dwarf. It is due to recombination processes of hydrogen being ionized by X–rays emitted from the accretion spot on the primary star. Its progression is the same as that of the BC, but phase–shifted by $\Delta\varphi \approx 0.25$.

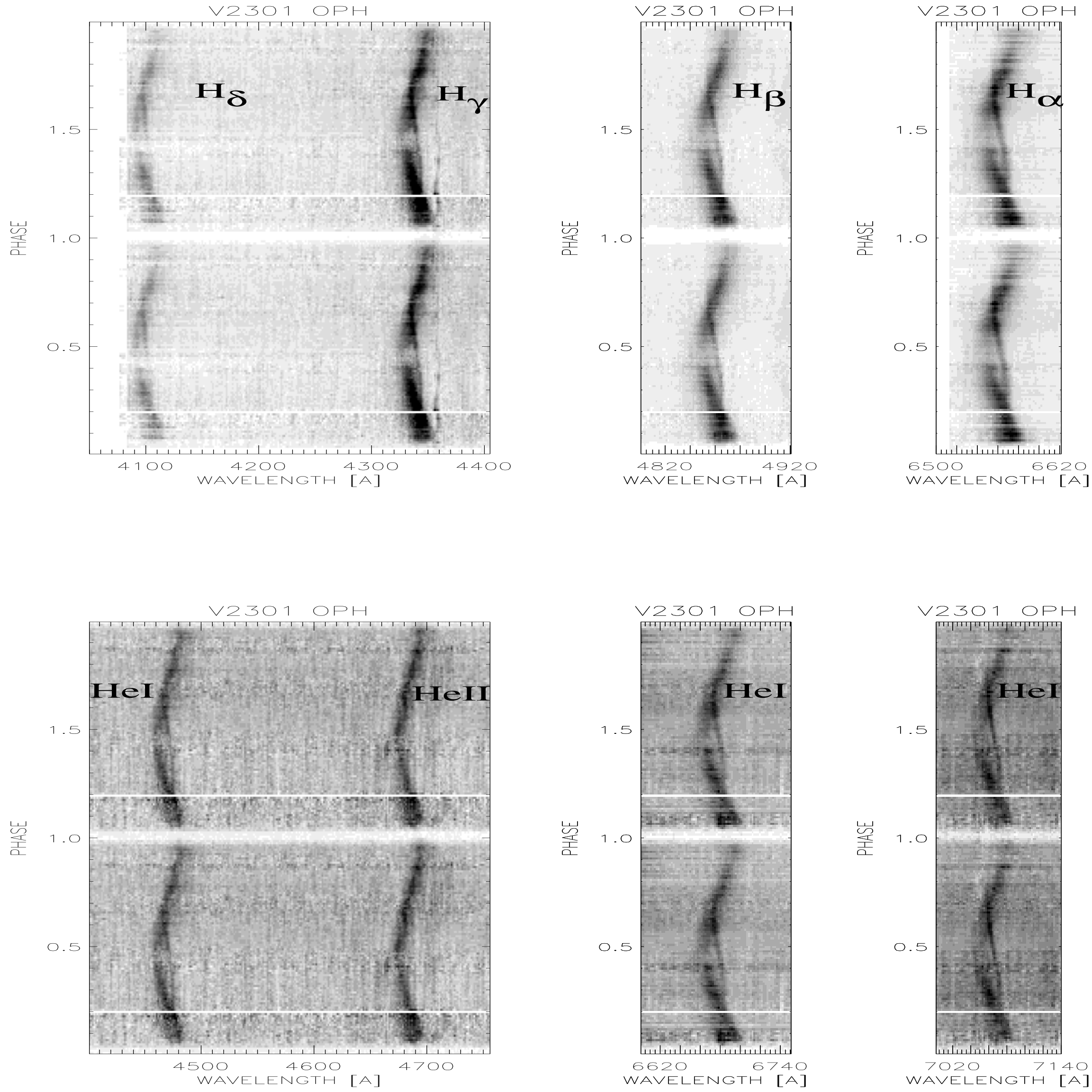

Fig. 1. Trailed, photometrically calibrated, high–resolution spectra of V2301 Oph derived by phase–averaging the spectra into 100 phase bins. The dynamic range of each gray–scale plot was chosen appropriately to emphasize the indiviual features of the emission lines, where the phase runs along the ordinate and the wavelength along the abscissa. Note, that the HeII (λ4686) emission line shows no narrow line component, indicating the origin of this line in the accretion column only. Another peculiarity is present in the HeI (λ7065) emission line, where the narrow component is still visible shortly before and after φ = 0.0, an effect not observed in other emission lines.

Therefore, the NC represents the orbital motion of the photocenter of the illuminated part of the secondary star. The profile of HeII (λ 4686) is different in not showing a narrow component. However, this behaviour seems to be very sensitive to the amount of the X–ray emisson coming from the white dwarf, since spectra obtained by Hessman et al. (1995) clearly do show the presence of the NC in the HeII (λ 4686) emission line. We therefore presume, that HeII (λ 4686) at this accretion state mostly originates in the gas stream.

Visible only in the trailed spectra is the weak, not resolved Bowen blend (NIII(λ 4634), NIII(λ 4641), CIII(λ 4650)). In CV's, the intensity of this line complex is correlated with that of HeII (λ 4686), with the Bowen blend being weaker, but not with such an extreme ratio. However, this behaviour seems not to be unusual in AM Hers since Schwope et al. (1996), presented trailed spectra of HU Aqr showing a similar ratio.

The most striking feature was observed in the HeI (λ 7065) emission line, whose NC is still visible shortly before and after φ = 0.0, an effect not observed in other emission lines, where the NC vanishes already around phase $\varphi \approx 0.8$. The eclipse of the NC seeems to be mostly symmetric to phase φ = 0.0. Due to the longer visibility of the NC, it is likely that most of the secondary's area facing the primary star is irradiated.

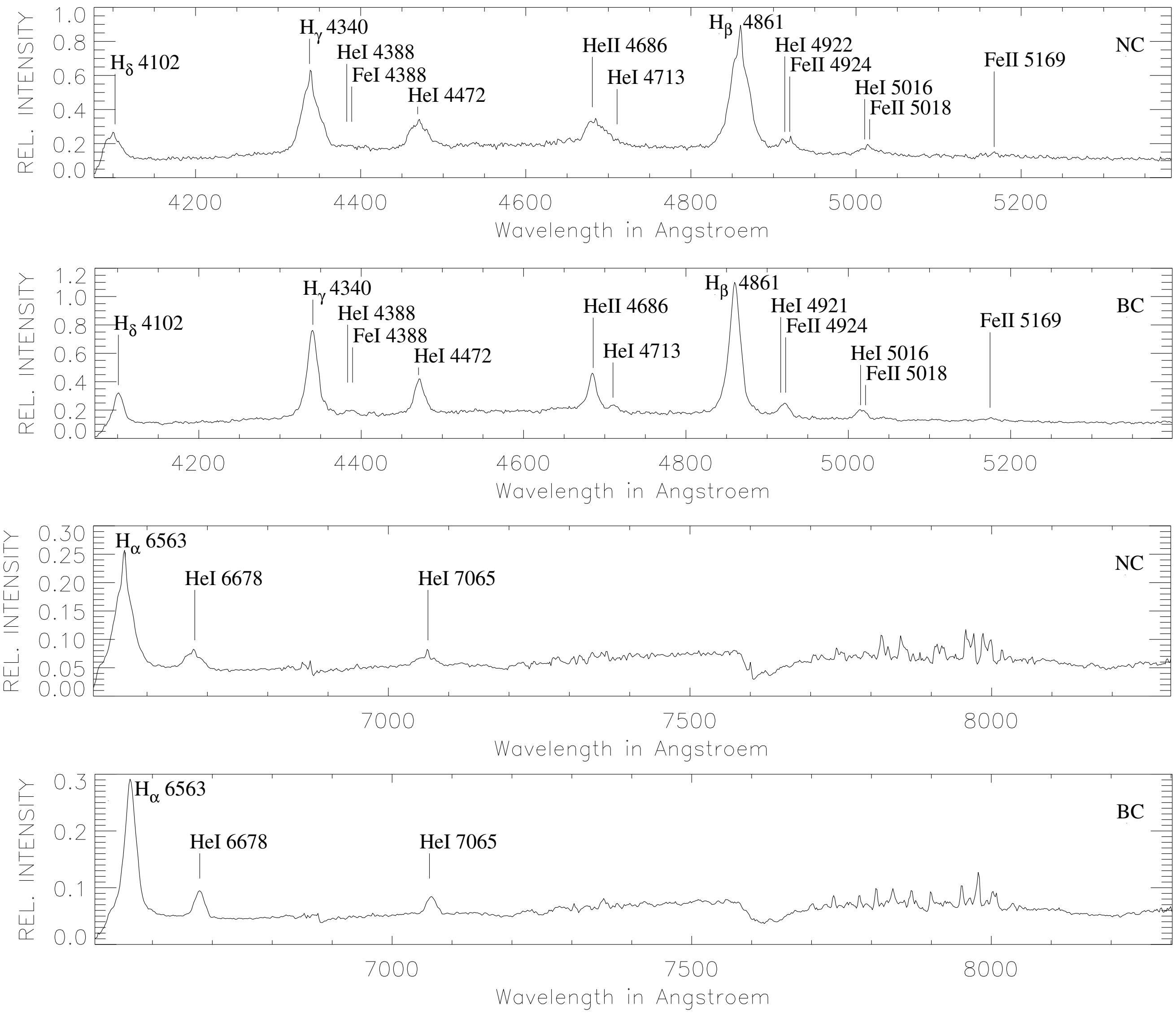

Fig. 2. Mean orbital spectra of V2301 Oph in the blue spectral range (upper both panels) and the red spectral range (lower both panels) after radial–velocity–correction, in order to emphasize either the NC (additional shift of 275 $\mathrm{kms}^{-1}\cdot\ \sin\phi$) or the BC (additional shift of 575 $\mathrm{kms}^{-1}\cdot\ \sin\phi$). The NC manifests itself in a spiky peak atop of the broad line wings, whereas the BC is represented by round, broad peaks. Note, that the HeII (λ 4686) shows no sign of a narrow component. The spikes around 6880Å and between 7200. . . 7380Å as well as 7700. . . 8180Å are faint remnants of atmospheric emission lines, whereas the feature at 7600Å represents the atmospheric oxygen absorption band.

3.2. The mean orbital spectra

In Fig. 2 we present radial velocity–corrected, mean orbital spectra in the blue (4080. . . 5350Å) and in the red spectral range (6500. . . 8300Å) in order to distinguish spectroscopic evidence either of the narrow component or the broad component. To accentuate either the NC or the BC the spectra were shifted with a radial velocity of -275 $\mathrm{kms}^{-1}\cdot\ \sin\phi$ and -575 $\mathrm{kms}^{-1}\cdot\ \sin\phi$, (both values taken from Barwig et al. 1994) respectively. The mean optical spectra of V2301 Oph are characterized by intense emission lines typical of an AM Her system in a high state.

We identified lines of the Balmer series (H_δ, H_γ, H_β and H_α) as well as of HeI ($\lambda\lambda$ 4388, 4921, 5016) blended with FeI ($\lambda\lambda$ 4388, 4924, 5018) and the single lines of HeI ($\lambda\lambda$ 4471, 4713, 6678, 7065) and HeII (λ 4686).

The NC–corrected spectra show a peaked narrow emission line atop the broad line wings except for HeII, where no spiky component could be detected. On the other hand the BC–corrected spectra exhibit round, broad line wings.

An additional proof for the high–state of this system is the invisibility of the KI and NaI absorption lines, which are typical for an M–dwarf secondary in such binaries.

3.3. Radial velocities

The usual procedure of measuring radial velocities in complex emission lines is fitting Gaussians to their line profiles.
Our investigation was restricted to the strong Balmer lines (H_γ, H_β, H_α), because of the poor S/N of the HeI and HeII lines. The H_δ emission line was omitted, since lying too close to the edge of the CCD. In each pixel row of the trailed spectra we fitted the NC and the BC with two Gaussians simultaneously. To suppress the influence of noise in these spectra and to provide a reliable profile fit, the central region of the Gaussians was given a bigger weight with respect to the adjacence (continuum–transition) of the line profiles.
After that, a sine–fit was applied to the fitted radial velocities V of the NC using the following relation :

$$V \;=\; \gamma - K_{NC}\, sin(\varphi - \varphi_0) \tag{1}$$

where γ is the system velocity, and K_{NC} denotes the radial velocity amplitude of the narrow component. φ and φ_0 respectively indicate the phase and the phase offset of the binary system.
The fitted radial velocities of the BC were approximated with a spline–curve. For the velocity amplitude K_{BC} of the highly variable broad component we could only estimate a value range between 600–650 kms^{-1}. Inaccurate measurements and broad scattering of the values occur during the phases, where the NC and BC intersect ($\varphi \approx 0.05 \ldots 0.2$ and $\varphi \approx 0.6 \ldots 0.8$).
These phase ranges were not taken into account, whilst measuring the velocities of the NC, in order to avoid falsification due to systematic errors.
The sine–fit to the radial velocity of the NC and the radial velocity curve of the BC are presented in Figs. 3 and 4, whereas the deduced values of K_{NC} and γ are displayed in Table 3.
By examining the system velocity γ it is apparent, that the derived values differ significantly from each other.
This might be explained physically with the probable blending of the H_γ and H_β emission lines with the HeII Pickering–series ($\lambda\lambda$ 4859,4339), an effect also observed for other AM Hers in high state e.g. for HU Aqr (Schwope et al. 1996).
The largest deviations could be found for the H_γ and H_β emission lines, so we take the γ of the unblended H_α as the appropriate value.
Also apparent is an increase of the K_{NC} values with the line excitation levels.
This is exactly the opposite what one would expect if those components are generated by irradiation from the vicinity of the white dwarf, as the photocenter of higher excitation lines should be closer to the L_1 point.
This increase in H_γ and H_β is ambiguous and probably results from distortions of the Gaussian fit, caused by nearby emission lines.
It should be stressed that the errors in Table 3 are estimated errors, assuming equal weighting for each Gaussian fitted radial velocity.
Determination of errors was done according to the procedure described in Bevington & Robinson (1992).

Table 3. Orbital parameter for V2301 Oph. K_{NC} is the amplitude of the radial velocity of the narrow component and γ denotes the system velocity, both in kms^{-1}. σ designates the errors of the mentioned parameter. H_{mean} is the deduced mean value of the radial velocity amplitude of H_γ, H_β and H_α from all observing nights. For further analysis the γ value of H_α was accepted to be the most reliable.

Line	K_{NC}	σK_{NC}	γ	σ_γ	Data
H_γ	329.90	6.20	-43.50	13.90	250
H_β	310.70	5.30	-107.80	7.60	348
H_α	300.80	2.60	-56.80	4.50	382

Line	$\overline{K_{NC}}$	$\overline{\sigma K_{NC}}$	Data
H_{mean}	307.40	2.70	980

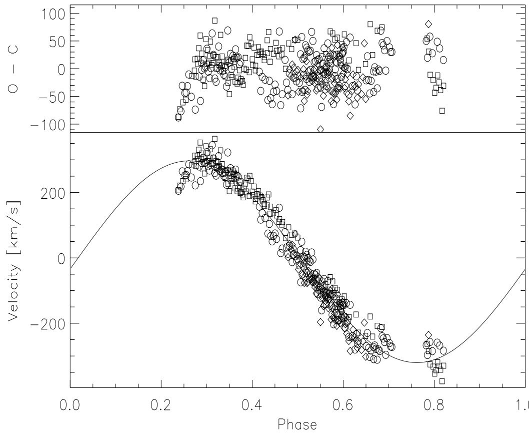

Fig. 3. A radial velocity curve for the narrow component determined by fitting Gaussians to the trailed spectra of H_α. The upper panel shows the residuals, the lower the distribution of the fitted data. The phase–range runs along the abscissa and the velocity along the ordinate. The solid line is the sine–fit to the data. Different symbols mark the three consecutive observing nights. The deduced radial velocities for each emission line are shown in Table 3.

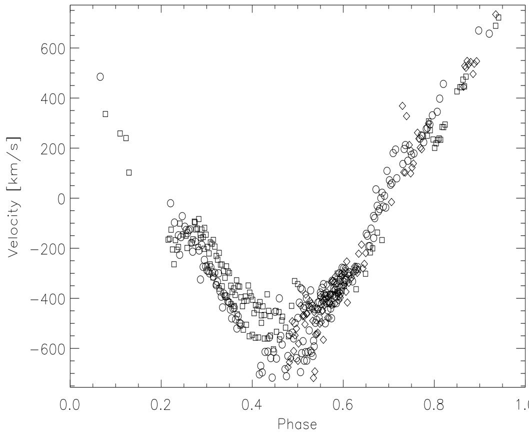

Fig. 4. Radial velocity curve for the broad component determined by fitting Gaussians to the spectra of H_α. The phase–range runs along the abscissa and the velocity along the ordinate. Different symbols mark the three consecutive observing nights. A spline approximation fitted to the data yielded an estimate for the radial velocity of the BC between 600 and 650 kms^{-1}.

3.4. Doppler tomography

Doppler tomography is an useful tool to extract further information on CVs from trailed spectra. This method which was developed by Marsh & Horne (1988) uses the velocity profiles of emission–lines at each phase to create a two–dimensional intensity image in velocity–space coordinates (V_X, V_Y).

Therefore, the Doppler tomogram can be interpreted as a projection of emitting regions in cataclysmic variables onto the plane perpendicular to the observer's view. The Doppler map is a function of the velocity (V_X, V_Y), where the X–axis points from the white dwarf to the secondary star and the Y–axis points in the direction of the secondary's motion. An image pixel with given velocity coordinates (V_X, V_Y) produces an S–wave with a radial velocity

$$V = \gamma - V_X\ cos(2\pi\phi) + V_Y\ sin(2\pi\phi) \tag{2}$$

where γ denotes the system velocity and ϕ the phase. Simply speaking, a Doppler map consists of a series of pixels comparable to a CCD–image, which was produced by summing up the line flux in the appropriate sinusoidals in the trailed spectra.

To accomplish this, a linear tomography algorithm, the fourier–filtered back–projection (FFBP) is used, which is described in detail e.g. by Horne (1991). The resulting Doppler map (or tomogram) is displayed as a grey–scale image. A helpful assistance in interpreting Doppler maps are additional inserted plots which mark the position of the secondary star and the ballistic trajectory of the gas stream. Assuming a Keplerian velocity field, emission originating near the center of the system has a larger velocity and thus appears in the outer regions of the map. Therefore, an image in such a representation is turned inside–out. For the tomogram analysis we restrict ourselves to the three Balmer lines H_γ, H_β, H_α and the interesting HeI ($\lambda\lambda$ 4471, 6678, 7065) and the HeII (λ 4686) emission lines. No reasonable Doppler maps could be produced either for H_δ, because this emission line was too close to the edge of the CCD, or for the blended HeI ($\lambda\lambda$ 4921, 5016) emission lines which had a poor S/N. Nevertheless, our data set exhibits a rich variety of seven emission lines from different temperature regions and excitation states. Since we cannot assume any relation between position and velocity during eclipse we constrained our data set by removing eclipse spectra between the phase–ranges $\phi = 0.01 \ldots 0.03$. Before computing the tomograms we subtracted the continuum from the individual emission–lines, since their line–flux is the quantity needed to produce these maps. This was done by subtracting from each pixel row of the trailed spectra the according median of the intensity. The emission lines in V, ϕ–coordinates are displayed in Figs. 6 and 8 and the corresponding Doppler maps in velocity coordinates (V_X, V_Y) are shown in Figs. 7 and 9 as grey–scale–plots.

Two general features can be easily recognized in each tomogram, an intense bright spot around velocity $V_Y \approx +300\ \mathrm{kms^{-1}}$, and an extended, bright region nearby that spot reaching out leftwards with velocity coordinates of $V_X \approx 0 \ldots - 1000\ \mathrm{kms^{-1}}$, $V_Y \approx 0 \ldots - 300\ \mathrm{kms^{-1}}$.

As explained above, the FFBP transforms every sine curve in the trailed spectra to points in the tomograms. The intense spot thus correlates to the NC, which represents the heated face of the secondary, whereas the extended, bright region corresponds to the BC. The distances of the NC and BC from the origin of the map correspond to the semi–amplitude of the according component.

It should be noted, that we achieved a FWHM resolution of 200 $\mathrm{kms^{-1}}$ in the central regions of the tomograms, whereas at higher velocities ($\approx$ 800 $\mathrm{kms^{-1}}$) the resolution of the maps suffered a considerable degradation.

Furthermore, the emission lines can be blurred by the so–called 'gamma–smearing' effect which is explained in detail by Diaz & Steiner (1994). Gas moving with a velocity perpendicular to the orbital plane V_Z generates a shift $\gamma = V_Z cosi$ which blurs the corresponding feature in the Doppler image in a ring–like manner.

The linear structures in the high velocity region of the map are sampling artefacts (aliasing streaks) which are not taken into account in the further interpretation. For a detailed discussion about sampling artefacts see e.g. Robinson et al. (1993).

The schematic overlay of the Roche–lobe and the gas stream trajectory is a function of K_1 and K_2.

We computed our trajectory by taking the best estimate for the mass ratio q ($M_1 \approx 0.897 M_\odot$ (primary star) as well as $M_2 \approx 0.185 M_\odot$ (secondary star)) from Barwig et al. (1994).

By using the following relation for the star masses (M_1, M_2) and their radial velocity amplitudes (K_1, K_2)

$$q = \frac{M_2}{M_1} = \frac{K_1}{K_2} \tag{3}$$

as well as using the radial velocity $K_2 = 400 \pm 50\ \mathrm{kms^{-1}}$ of the mass center of the secondary, measured from absorption lines when the system was in a low state (Barwig, in preparation), we were able to evaluate the missing value $K_1 \approx 82\ \mathrm{kms^{-1}}$ for our schematic overlay. The center of mass and the location of the white dwarf are marked respectively by a cross and a point located below the Roche lobe, whereas the stream is represented by an arc originating from the secondary's lobe at the inner Lagrangian point. This arc is calibrated every $0.1 R_{L_1}$ (open circles) as it accelerated towards the primary star.

Due to the magnetic field geometry the stream moves only at the beginning along a ballistic trajectory and is then deviated left–downwards.

In order to compute the magnetically funnelled trajectory one needs to know two parameters, the azimuthal angle ψ and the inclination angle θ of the white dwarf's magnetic pole from the rotational axis.

The azimuthal angle ψ (angle between the direction from the primary to the secondary star and the projection of the gas stream onto the orbital plane) corresponds to the phase shift ($\Delta\phi$ = 0.25) between the narrow component and the broad component. Since the Doppler tomograms are virtually blind towards vertical motions we used the values of Ferrario et al. (1995) to estimate θ.

According to Ferrario et al. (1995) the best fit of the viewing angle to the dipole axis is estimated to be about 70°, so the colatitude of the magnetic pole is expected to lie between 15° and 30°, depending on the assumed orbital inclination.

The resulting magnetically funneled trajectory moves within the emitting regions of the BC in the Doppler maps.

Note, that it also might be possible, that this weak magnetic AM Her is accreting material onto the other magnetic pole. Some features in our Doppler maps (especially H_γ) indicate such a behaviour, where the intensity distribution can be fitted with a magnetically funneled accretion stream onto the opposite pole, using the same, but negative θ–value. This trajectory is plotted in the H_γ Doppler tomogram, although we cannot rule out that the emission feature near the inner Lagrangian point might as well come from an almost stationary component with a low velocity amplitude like in V834 Cen (Rosen et al. 1987). Theoretical and geometrical calculations considering accretion onto both poles were performed by Ferrario et al. (1989).

We generally assume, that most of the emission of the BC is coming from or originating near the coupling region. The ballistic trajectory hardly fits any of the bright emission spots of the BC and the V_X and V_Y velocity values are too high to represent a free–falling gas stream near the inner Lagrangian point L_1.

We could not calculate the trajectories behind the coupling region, because the accretion kinematics are not well known there. Even so, every tomogram shows its own interesting features which are explained below.

A position coordinate display of the system and the different trajectories are shown in Fig 5. The eclipse–removed, continuum–subtracted trailed spectra used for computing the Doppler maps are displayed in velocity–coordinates in Figs. 6 and 8, respectively.

The tomogram of H_γ (Fig. 7) shows an intense small spot (NC) around $V_Y = 300$ kms^{-1} and a bright, extended region (BC) extending leftwards from it with velocity coordinates of $V_Y = 0 \ldots - 400$ kms^{-1} and $V_X = 0 \ldots - 1000$ kms^{-1} .

Another interesting feature is the part of the stream which seems to combine the gas stream and the secondary. This might be interpreted as an emission contribution originating near the inner Lagrangian point. From this map we considered an accretion onto the opposite pole.

Therefore, the magnetically funneled trajectory moves in a direction opposite to the ballistic one. The bright area with the intense spots inside depicts the gas stream which is compressed before being coupled on the magnetic field line.

Comparing the H_β with the H_γ (Fig. 7) Doppler map, we find some differences. The secondary's feature is more intense and the bright area is stronger than in the H_γ map, confirming the higher intensity of H_β.

The H_α tomogram (Fig. 7) seems to be more blurred which may be due to the above mentioned 'gamma–smearing' effect, but we can still distinguish the same features (bright spot and extended bright area) as in the other maps. The Doppler maps of the Helium emission lines display weaker features.

In the HeI (λ 4472) tomogram (Fig. 9) the same small intense spot (illuminated face of the secondary) can be found, whereas the gas stream is represented by a bright, fragmented area extending leftwards from the spot.

One of the most interesting tomograms resulted in back–projecting the HeII (λ 4686) emission line (Fig. 9) where the NC is absent. Thus, we are able to compute a map representing the BC only. Instead of the secondary's feature we could only detect a diffuse area resulting from the back–projection of the adjacent HeI (λ 4713).

An intense bright spot is present with velocity coordinates of $V_X \approx 0 \ldots - 800$ kms^{-1} and $V_Y \approx 0 \ldots - 400$ kms^{-1} which is due to emission lines originating in the coupling region.

The Doppler map of HeI (λ 6678) (Fig. 9) represents the same but weaker features as the Balmer lines, whereas the last but not the least interesting tomogram presented by the HeI (λ 7065) emission line (Fig. 9) shows a stronger NC than in other maps.

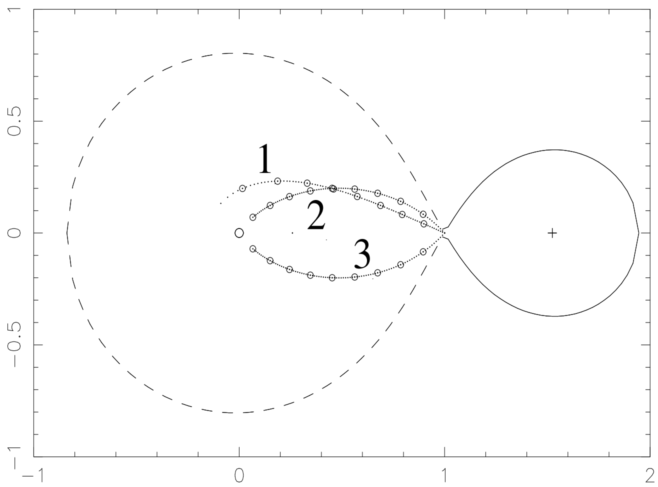

Fig. 5. Position coordinate display of the accretion geometry of V2301 Oph computed for an assumed mass ratio of $q = 0.205$. The loci of the secondary and the primary star are denoted by a cross and a point, respectively. Their Roche lobes are displayed as solid (secondary) and dashed lines (primary). The axes are plotted in units of the distance between the white dwarf and L_1. The ballistic trajectory (stream 1) is plotted together with the magnetically funneled part of the stream computed for $\psi = 25°$ and $\theta = 70°$ (stream 2). Additionally, we inserted a magnetically funneled trajectory (stream 3) computed with a negative θ–value for accretion on the opposite pole.

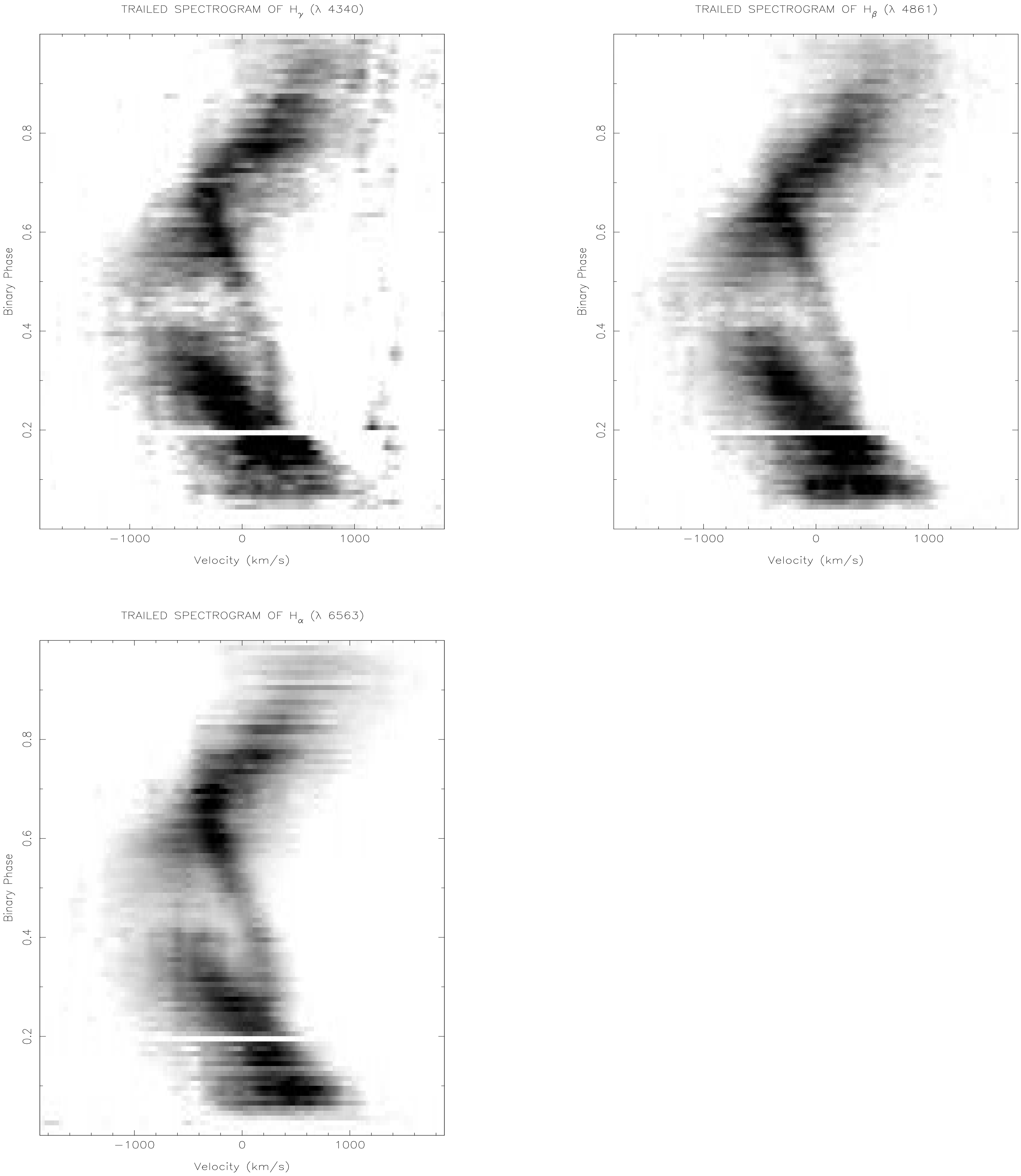

Fig. 6. Zoomed gray–scale representations of continuum–subtracted, photometrically calibrated, high–resolution spectra of the prominent Balmer lines H_γ, H_β and H_α. The emission lines are plotted in v, ϕ–coordinates. Not covered phase–ranges are marked with white empty rows. The eclipse spectra have been removed, since we assume no relation between position and velocity.

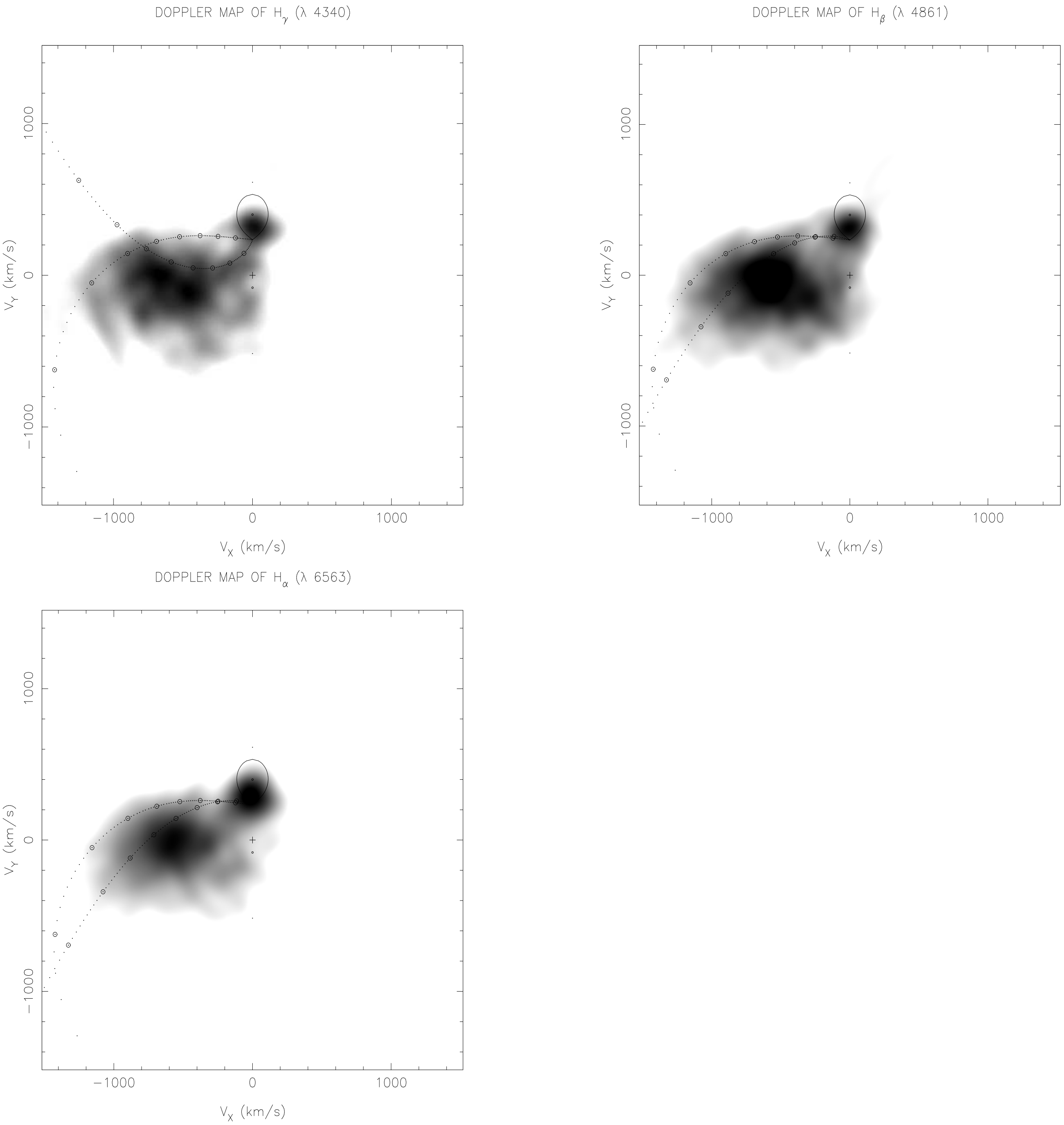

Fig. 7. Doppler maps of the prominent Balmer lines H_γ, H_β and H_α in velocity space (V_X, V_Y) using the Fourier–filtered back–projection technique. The intense small spot around V_Y = 300 kms^{-1} represents the heated face of the secondary, whereas the gas stream is denoted by the bright area extending leftwards from the spot with velocity coordinates $V_X \approx 0 \ldots -1000$ kms^{-1}, $V_Y \approx 0 \ldots -400$ kms^{-1}. Sampling errors are represented by aliasing streaks in the higher velocity regions. A schematic overlay marks the Roche–lobe of the secondary, the ballistic trajectory and the magnetically funneled horizontal part of the accretion stream. Note, that in the H_γ map, a magnetically funnelled trajectory has been modelled, assuming an accretion to the opposite pole. Further information for each line is given in the text.

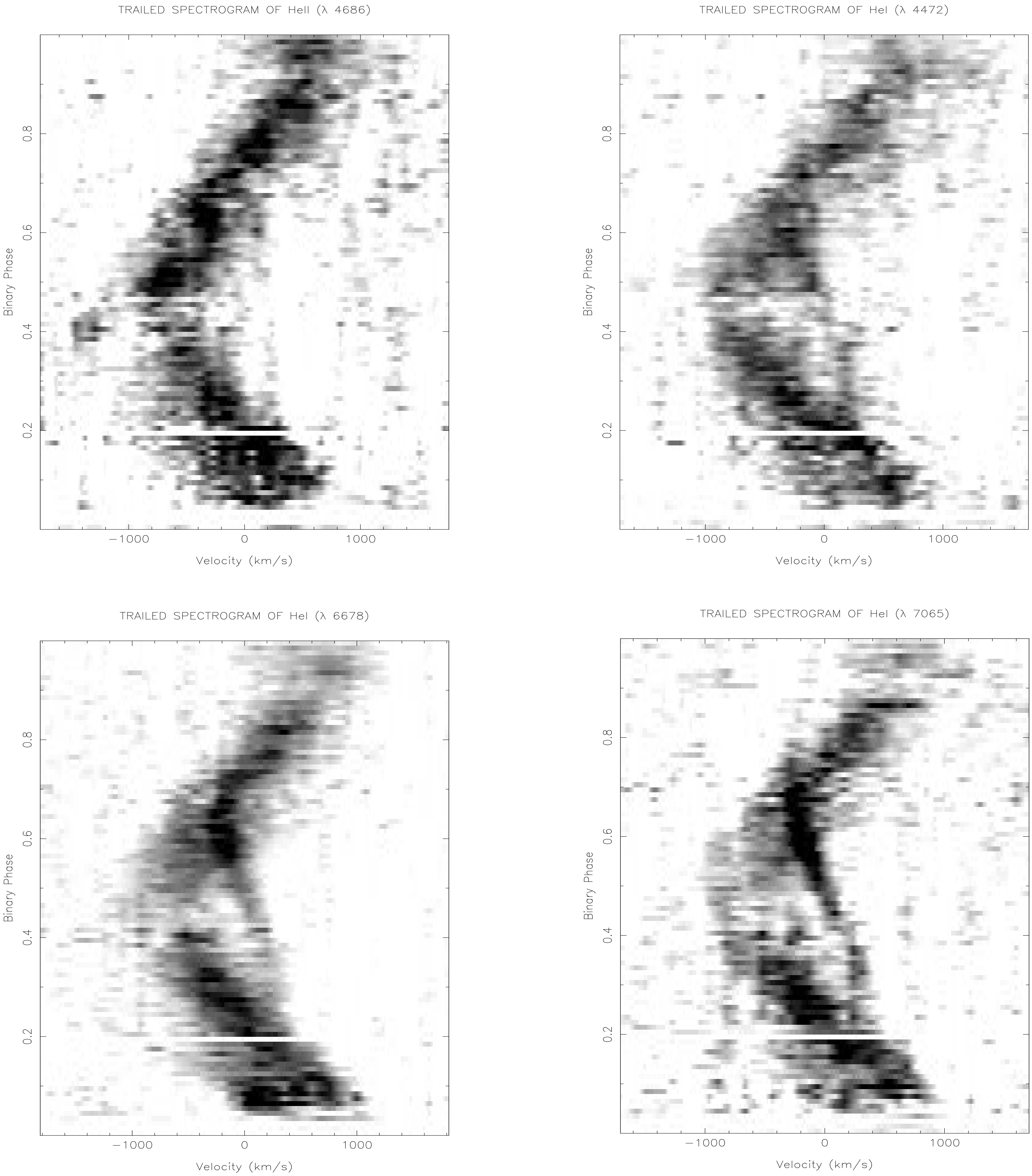

Fig. 8. Zoomed gray–scale representations of continuum–subtracted, photometrically calibrated, high–resolution spectra of the weaker lines HeII(λ 4686), HeI(λ 4472), HeI(λ 6678), HeI(λ 7065) . The emission lines are plotted in υ, ϕ–coordinates. Empty phase–ranges are marked by blank rows. Eclipse spectra have been removed, since we assume no relation between position and velocity. Note, that the NC in the HeI (λ 7065) emission line is still visible shortly before and after phase $\varphi = 0$.

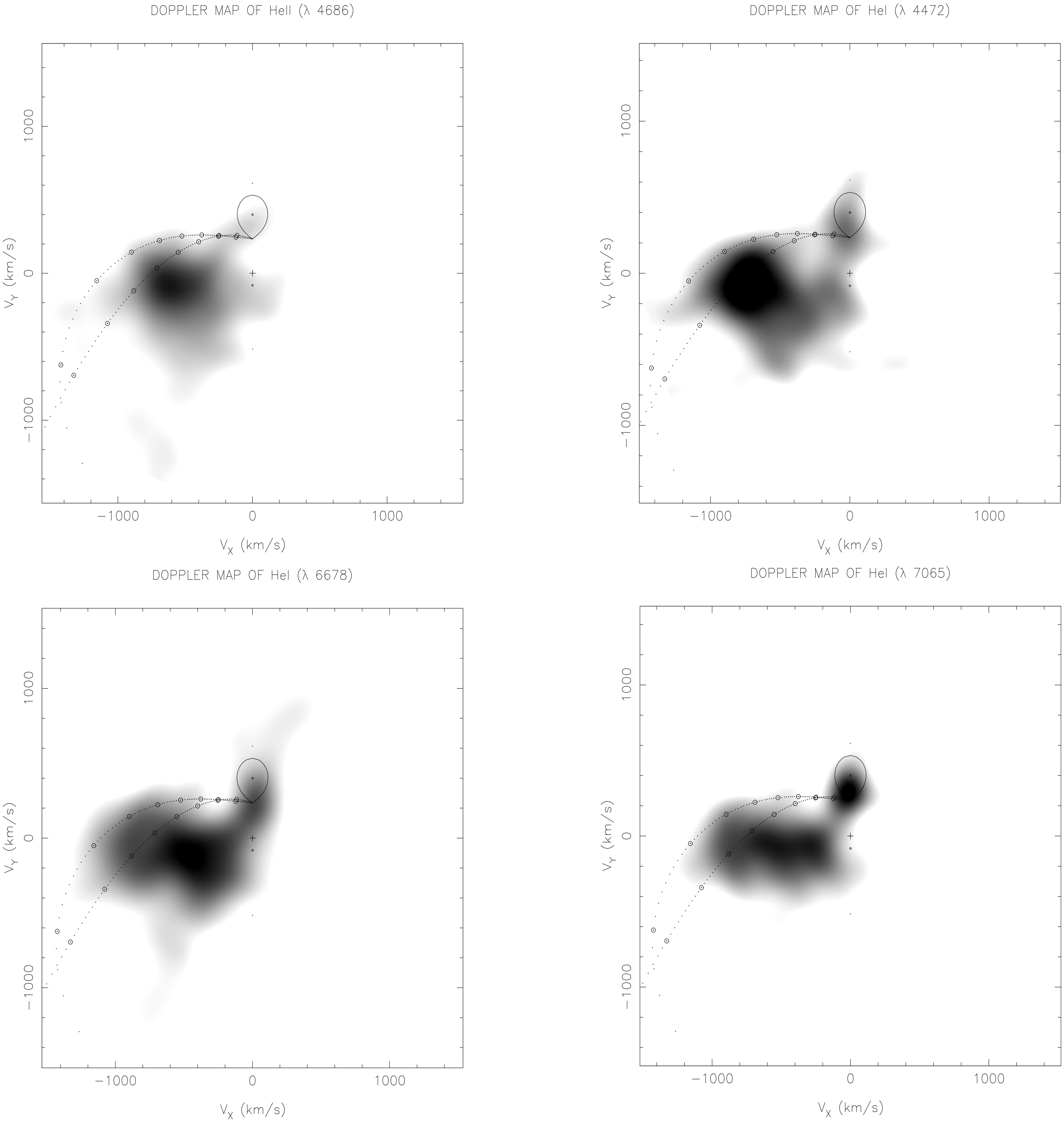

Fig. 9. Doppler maps of the HeII(λ 4686), HeI(λ 4472), HeI(λ 6678), HeI(λ 7065) emission lines, computed by the Fourier–filtered back–projection algorithm. The data set is presented in velocity coordinates (V_X, V_Y). Again, the irradiated face of the secondary is represented by the small, intense spot around V_Y = 300 kms^{-1}, whereas the accretion column manifests itself in the bright, sometimes diffuse area moving away leftwards from the spot with velocity coordinates $V_X \approx 0 \ldots - 1000$ kms^{-1}, $V_Y \approx 0 \ldots - 400$ kms^{-1}. A schematic overlay marks the Roche–lobe of the secondary, the ballistic trajectory and the magnetically funneled horizontal part of the accretion stream . Sampling errors are represented by aliasing streaks at higher velocities. Further explanations for each line are given in the text.

3.5. The light curves

Spectrophotometric observations of V2301 Oph were obtained with MEKASPEK over three consecutive nights (06–09 Aug., 1994) and in the night of 04/05 Aug., 1994. Seven eclipses could be acquired, though only the last night turned out to be photometric. The data set was reduced as described in Sec.2.1. and then phase–folded with a time resolution of 1s using the updated eclipse–ephemeris (see Sec.2.1.). The reduced light curves of each night in integral light are presented in Fig. 10. Several quite interesting features of the light curve are explained in the following.

A well–known feature (Barwig et al. 1994) is the two-stepped eclipse ingress/egress of the white dwarf and the gas stream. In the first ingress step, the white dwarf is occulted, whereas the temporally highly variable accretion column is eclipsed during the second ingress step. The following progression of the light curve is flat, indicating a total eclipse of both components. After that, the primary star emerges first, pictured in the first egress step, followed by the gas stream which reappears in the second step. Another interesting feature is the pre–eclipse hump between phases $\phi \approx 0.5 \ldots 0.85$. Such a behaviour cannot be explained with the common hot spot–accretion disc configuration. Barwig et al. (1994) concluded that the observed ingress/egress phases of an assumed hot spot would require an unrealistically small accretion disc. Superimposed on the hump and the remaining out–of–eclipse light curve is a non–periodic, sometimes quasi–periodic flickering, which might have its origin in the hot, anisotropically radiating gas stream.

The duration of the eclipse of the white dwarf was measured in the B–channel by smoothing the eclipse features (ingress/egress steps) of every single night with an approximating spline first, and taking the derivative of this fit afterwards. Derivatives of ingress and egress features show local minima and maxima, respectively. Those quite precise time values with an error corresponding to the time resolution, were taken to determine the timings of the ingress/egress of the primary star. The individual values for each night as well as the average eclipse times are given in Table 4.

Table 4. Ingress, egress times and eclipse duration of the white dwarf

Date	ingress (HJD 2449569 +)	egress (HJD 2449569 +)	ecl.dur. (sec)
04/05.08.1994	0.413130	0.417781	402
06/07.08.1994	2.452687	2.457428	409
07/08.08.1994	3.394128	3.398908	413
	–	3.477306	–
	3.551054	3.555700	401
08/09.08.1994	4.413955	4.418685	409
	4.492329	4.497157	417

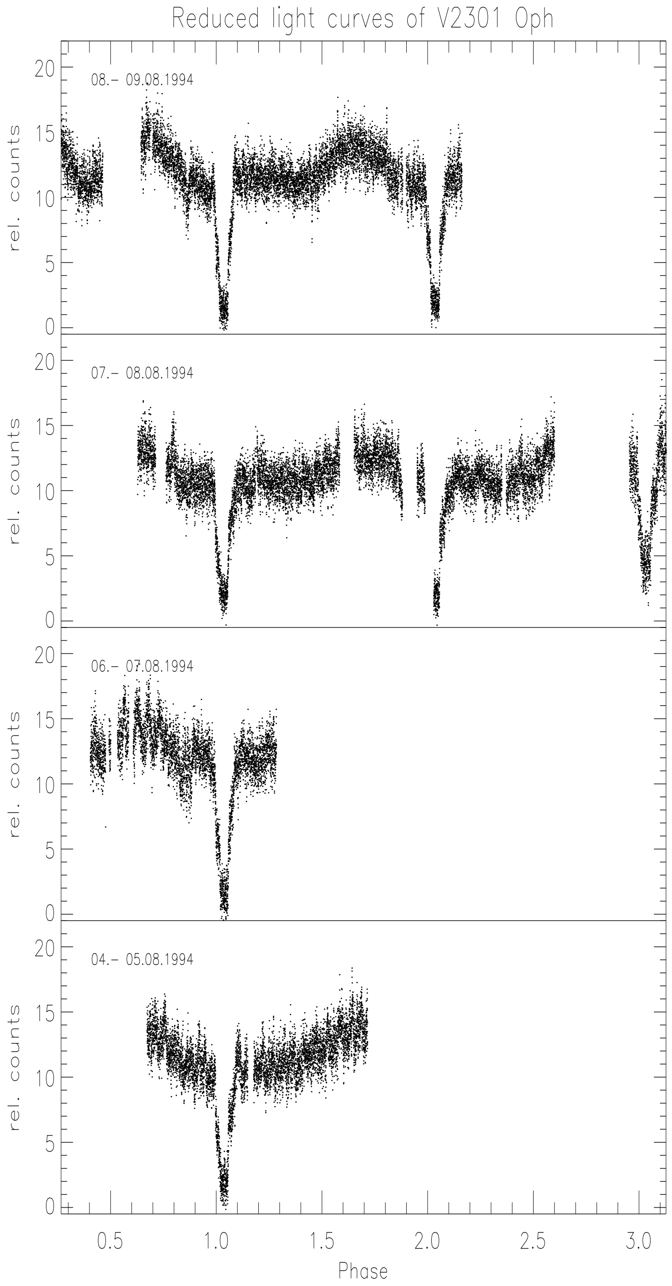

Fig. 10. Reduced light curves of V2301 Oph in integral light taken on the indicated dates. Gaps within the light curves are due to calibration measurements. The same scaling of the Y–Axis has been taken for all plots, because we wanted to check night to night flux variations. Every data point represents an intergration of 1s. The main features, two–stepped eclipse ingress/egress and the pre–eclipse hump (explained in Sec.3.5.) as well as the superimposed flickering are clearly visible. More information is given in the text.

3.6. The decomposition of light curves

As explained in Sec.2.2., using MEKASPEK we were able to extract Balmer lines from the continuum. Emission lines of V2301 Oph are thought to be arising mainly in the gas stream and on the illuminated face of the secondary, whereas the white dwarf dominates in the continuum.

The decomposed light curves have a lower time resolution (20s), in favour of a better S/N. Still, the signal is quite noisy and useful information can only be obtained by phase–folding all acquired light curves at the orbital period. In order to increase the S/N, the individual phase diagrams of the Balmer lines and the underlying continuum were summed up as shown in Fig. 11. The continuum light curves show features of the primary star, whereas the pre–eclipse hump between phase ranges $\phi \approx 0.5 \ldots 0.8$ can be assigned to radiation coming from the shock region on the white dwarf. Cyclotron emission from the accretion spot might also contribute to this feature (Schwope, private communication). Note, that the pre–eclipse hump is quite weak in the following analysis of the emission line light curves.

The light curves of the Balmer lines differ significantly from those of the continua. Between phase ranges $\phi \approx 0.7 \ldots 0.9$ a continuous decrease of the lightflux is observed. This can be explained with the revolving of the secondary's irradiated face off the line–of–sight on the one hand, and with the progressing obscuration of the gas stream by the secondary star on the other hand. The intensity drop at the beginning of the eclipse (phase $\phi \approx 0.0$) is steep and short in duration. It can be interpreted as the eclipse of the remaining part of the accretion column by the secondary star and serves also as a clear evidence that the accretion stream is distorted due to a weak magnetic field of the primary star.

Another interesting feature only present in the emission line light curves is a second, weaker eclipse, ocurring around phases $\phi \approx 0.3 \ldots 0.5$. This can be explained as self–obscuration of the gas stream. We restricted this second eclipse to the accretion stream mostly, because after cross–checking the light curves with our trailed spectra we found out that the intensity flux of the BC was decreasing at the same phase range, whereas the NC remained at its normal flux. Due to its stronger signal, the spectrophotometric emission line phase–light curves are dominated by the BC.

To provide an even more detailed look and to check our calibration method we derived spectroscopic light curves from the emission lines of our photometrically calibrated high–resolution trailed spectra. These light curves taken from H_δ, H_γ, H_β and H_α in Fig.12, as well as the HeI ($\lambda\lambda$ 4472, 6678) lines in Fig.13 show the same appeareance as the spectrophotometric light–curves with only H_δ being noisier, because this line resided close to the edge of the CCD chip.

An effect only visible in these high–resolution light–curves is, that the ingress/egress asymmetry has its origin in the BC.

The short increase in intensity around phase $\varphi \approx 0.05 \ldots 0.1$ can be contributed to the inner, concave side of the accretion column, which is illuminated by the reprocessed radiation of the white dwarf.

An interesting exception is again HeII (λ 4686) (see Fig. 13), which shows a considerably steeper ingress, due to the missing contribution of the illuminated face of the secondary star.

On the other side, a shorter and symmetric V–like eclipse for HeI (λ 7065) can be recognized in Fig.13, because of the dominant presence of the NC.

By smoothing the emission line and continuum light curves with an approximating spline and again computing the derivative, we confirmed the eclipse of the white dwarf happening before the eclipse of the accretion stream. Because of this time–delay, we conclude that the magnetic dipole is inclined towards the orbital plane, resulting in a deviation of the gas stream.

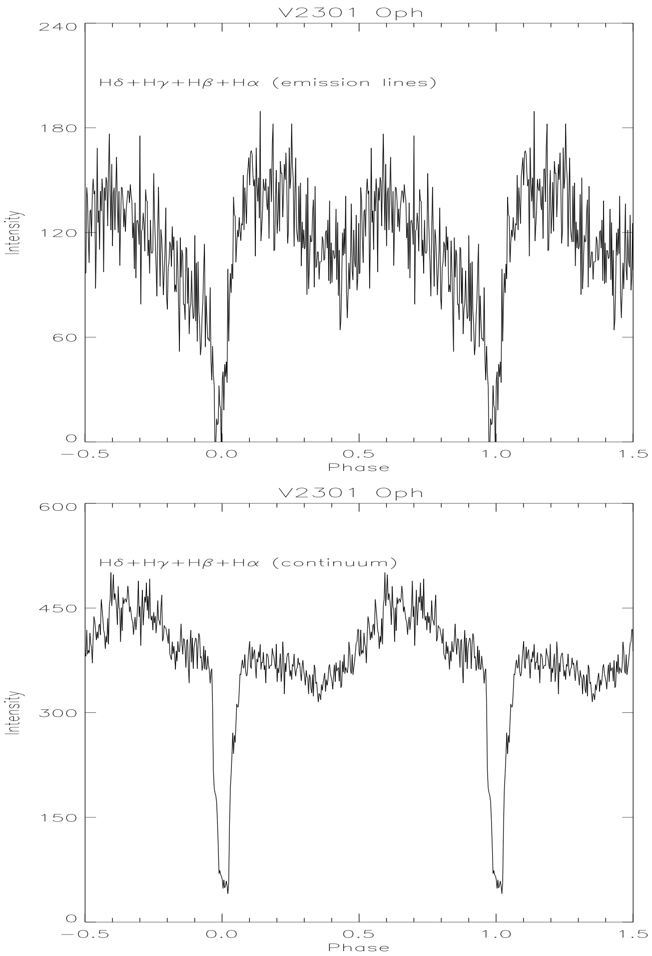

Fig. 11. Summed phase diagrams for the emission lines H_δ, H_γ, H_β, H_α (upper panel) and for the underlying continuum (lower panel). Integration time and bin size are 20s. Note, that the higher count rates result from the different type of reduction. Instead of calculating the object brightness relative to a comparison star, we only subtracted the sky–background. The phase–range is repeated for clarity and count rates are set to an appropriate value for each component in order to emphasize the special features of the contributing light sources. The overall appeareance of the emission line light curve differs significantly from the continuum light curve. A continuosly slow eclipse ($\varphi \approx 0.7 \ldots 0.9$) and a second eclipse ($\varphi \approx 0.3 \ldots 0.6$) can be contributed to: a) the obscuration of the accretion stream by the secondary star and b) the obscuration of the accretion column by itself. See Sec. 3.6 for a more detailed information.

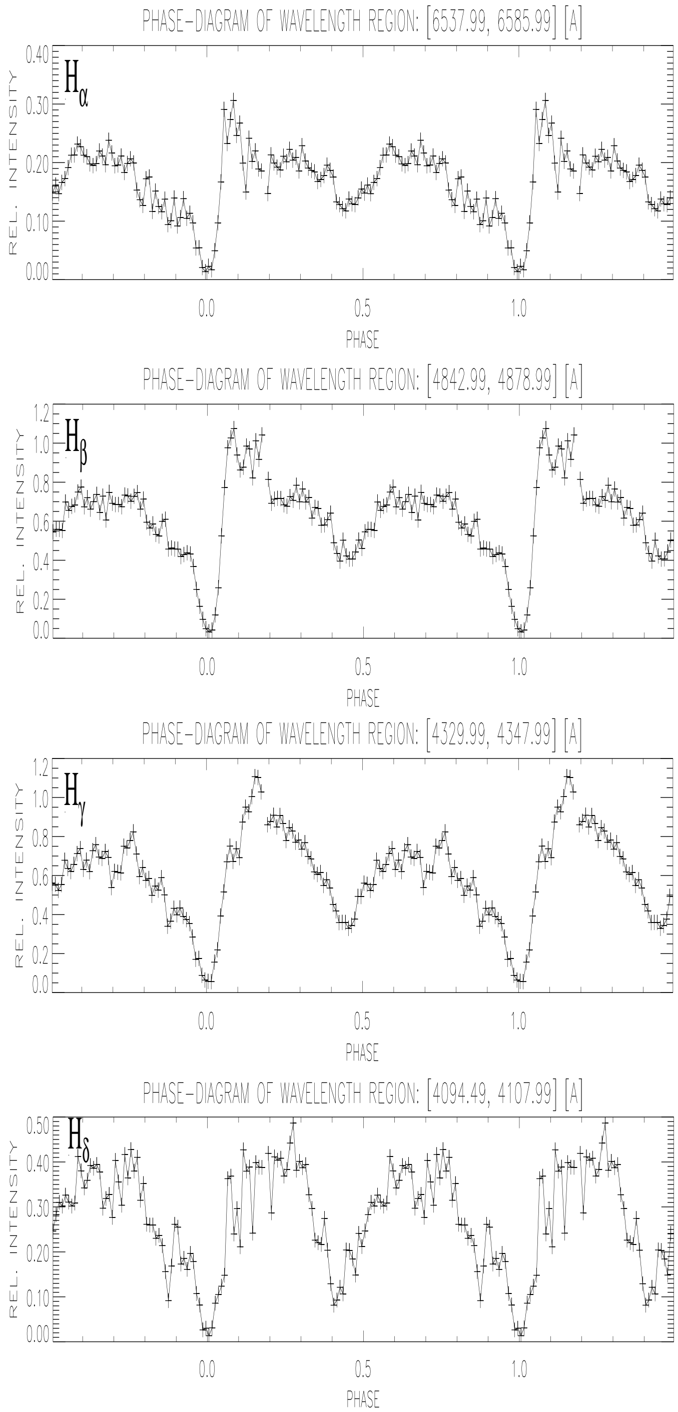

Fig. 12. Spectroscopic light curves of V2301 Oph (from bottom to top: H_δ, H_γ, H_β, H_α), extracted from the wavelength ranges indicated on the headline of each plot. Integration time corresponds to the bin size (1 bin $\approx$ 1.13min). Not covered phase ranges ($\phi \approx 0.2$) appear as gaps. The progression of the light curve is consistent with our simultaneously taken spectrophotometric data.

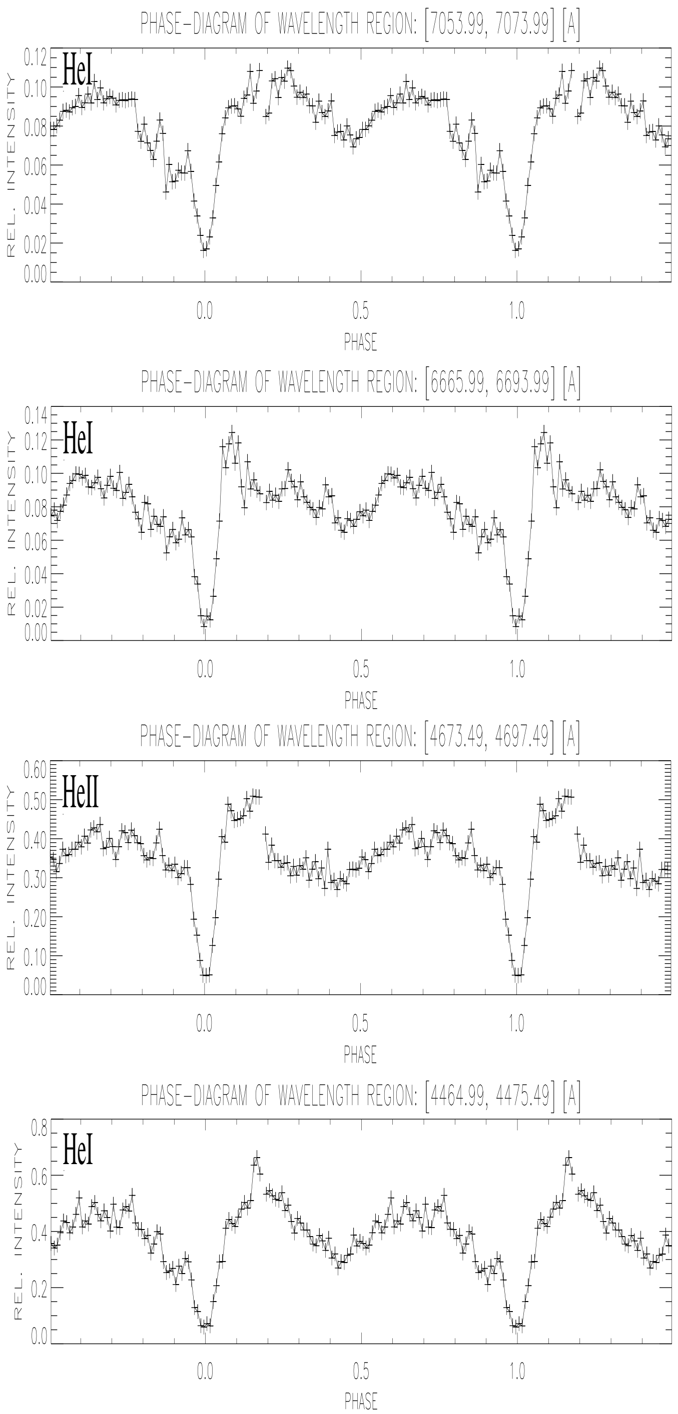

Fig. 13. Spectroscopic light curves of V2301 Oph, (from bottom to top: HeI (λ4472), HeII (λ4686), HeI (λ6678), HeI (λ7065)) extracted from the wavelength ranges indicated on the headline of each plot. Integration time corresponds to the bin size (1 bin $\approx$ 1.13min). Not covered phase ranges ($\phi \approx 0.2$) appear as gaps. The progression of the light curve is consistent with our simultaneously taken spectrophotometric data. Note the peculiarities in the HeII phase–light–curve, which shows a steep ingress due to the missing contribution of the NC, as well as in the HeI (λ7065) phase light–curve, which shows a comparably shorter eclipse, because of the dominant presence of the NC.

4. Discussion and conclusions

We have presented high–resolution spectroscopy and high–speed–spectrophotometry of the AM Herculis star V2301 Oph during its high accretion state. By combining the two observational methods we were able to calibrate the continuum of the spectroscopic data set with the atmospheric–extinction–free continuum of the reduced spectrophotometric data set. Thus, it was possible to investigate separately emission line and continuum light curves. Our intention was to clarify the different classifications of this system as a low–field intermediate polar or an AM Herculis binary.

The analysis and interpretation of our data set favour an AM Her system with a weak and oblique magnetic field as proposed by Barwig et al. (1994) and Ferrario et al. (1995).

We could find no evidence for a small accretion disk, characteristic for a low–field intermediate polar in our spectroscopic data. The trailed spectra show no rotational disturbance during eclipse and the mean orbital spectra are single peaked. The appearance of strong Balmer emission lines in combination with emissions of HeI and of the prominent high–excitation HeII line are characteristic of an AM Her binary in a high accretion state. Another evidence for this classification are the complex emission line profiles which exhibit two components, a narrow one (NC) and a broad one (BC) phase–shifted by $\Delta\varphi \approx 0.25$ to each other. With the means of Doppler tomography the origin of the NC could be clearly located on the secondary star, whereas most of the BC arises in regions where the gas stream is compressed before being coupled onto the magnetic field lines of the primary star. This overall spectroscopic behaviour is in agreement with the standard model of AM Hers as outlined in e.g. Rosen et al. (1987).

Furthermore, we did also not detect any hints of a low–field intermediate polar in our photometric data set.

The pre–eclipse hump visible between phase $\varphi \approx 0.5 \ldots 0.8$, prior to the double–stepped eclipse ingress/egress of the white dwarf and the accretion stream, cannot be assigned to a hot spot on an accretion disc. Moreover, this feature, outstandingly visible in the continuum light curve, is a signature of cyclotron radiation coming from the shock region, where the gas stream impacts on the primary's surface. Emission line light curves reveal a shallow eclipse ingress and a steep eclipse egress contrary to the typically V-shaped eclipses of accretion discs. The shallow eclipse ingress feature beginning at phase $\phi \approx 0.7$, can be interpreted as the revolving of the secondary's irradiated face off the observers line–of–sight, and the succcesive obscuration of the remaining gas stream. The steep eclipse egress feature is due to the reappearing illuminated, inner side of the gas stream. Therefore, considering the high inclination (i$\approx 80^\circ$) and the just described sequence and progression of the eclipse features, we conclude that the presence of a small accretion disk is very unlikely.

We could also not detect any short periodic variations in the light curves which would indicate a not synchronously rotating white dwarf in an IP system. It should also be noted that this system has never been observed to undergo outburst states. Moreover, a long–term variability of 148d in the light flux, in order of up to 1^m (Antipin & Shugarov 1995), is a typical indicator for the low/high states of AM Her systems. Observations of this system in low state (Barwig, in preparation) show only the presence of the primary star (photometry) and secondary star (spectroscopy), respectively.

All the mentioned properties affirm the classification of V2301 Oph as an AM Herculis system.

Acknowledgments

The authors would like to acknowledge assistance and fruitful discussions from Alex Fiedler, Hauke Fiedler and Hans–Christoph Thomas. In particular we are grateful to Axel Schwope for his comments on an earlier draft, to an anonymous referee for helpful remarks on the manuscript and to Rick Hessman for useful advice during the observation run.

References

Antipin S.V., Shugarov S.Yu., 1995, In: Proceedings Abano–Padova Conference on Cataclysmic Variables, Kluwer Academic Publishers, p. 145
Barwig H., Schoembs H., Buckenmayer C., 1987, A&A 175, 327
Barwig H., Ritter H., Bärnbantner O., 1994, A&A 288, 204
Bevington P.R., Robinson D., 1992, Data reduction and error analysis for the physical sciences, McGraw–Hill Inc., New York.
Biermann P., Schmidt G.D., Liebert J., et al. , 1985, ApJ 293, 303
Diaz M.P., Steiner J.E., 1994, A&A 283, 508
Ferrario L., Wickramasinghe D., 1993, MNRAS 265, 605
Ferrario L., Wickramasinghe D., Tuohy I.R., 1989, ApJ 341, 327
Ferrario L., Wickramasinghe D., King A.R., 1993, MNRAS 260, 149
Ferrario L., Wickramasinghe D., Bailey J., Buckley D., 1995, MNRAS 273, 17
Hessman F.V., Beuermann K., Burwitz V., Reinsch K., Thomas H.C., 1995, In: Proceedings Abano–Padova Conference on Cataclysmic Variables, Kluwer Academic Publishers, p. 162
Horne K., 1986, PASP 98, 609
Horne K., 1991, In: Fundamental Properties of Cataclysmic Variable Stars: 12th North American Workshop on Cataclysmic Variables and Low Mass X–ray Binaries, San Diego, San Diego State University Publication, p. 160
Mantel K.H., Barwig H., 1993, NATO ASI series C436, 329
Mantel K.H., Barwig H., Kiesewetter S., 1993b, AG Abstract series 9, 14
Marsh T.R., Horne K., 1988, MNRAS 235, 269
Mukai K., 1988, MNRAS 232, 175
Robinson E.L., Marsh T.R., Smak J.I., 1993, In: Accretion Disks in Compact Stellar Systems, Singapore, World Scientific Publishing Co. Pte. Ltd, p. 75
Rosen S.R., Mason K.O., Córdova F.A., 1987, MNRAS 224, 987
Silber A.D., 1992, Ph.D.thesis, Massachusetts Institute of Technology
Silber A.D., Remillard R.A., Horne K., Bradt H.V., 1994, ApJ 424, 955
Schwope A.D., Mantel K.H., Horne K., 1996, A&A (in press)
Young P., Schneider D.P., 1979, ApJ 230, 502

This article was processed by the author using Springer-Verlag LaTeX A&A style file *L-AA* version 3.